Pitch stabilisation and longitudinal control of a hummingbird-inspired drone using an active tail

Arno Melis*, Jeroen Vanpoucke, Thomas Roelandt, Jan Swevers, Dirk Vandepitte
KU Leuven, Celestijnenlaan 300 box 2420, 3001 Leuven, Belgium

http://www.imavs.org/

ABSTRACT

This paper examines the use of an active tail for pitch stabilisation and longitudinal control of a hummingbird-inspired flapping-wing drone. The tail is positioned underneath the wings such that actuation of the tail angle redirects the airflow underneath the wings, resulting in a pitch control torque. A tail model derived from actuator disc theory and the blade element method is integrated into a free-flight simulation framework for longitudinal flapping-wing flight. Simulation results demonstrate that a linear quadratic regulator effectively stabilises the system and tracks a desired pitch angle. By incorporating velocity and position PI controllers in a cascaded architecture, the drone is additionally able to follow a longitudinal position reference. Experimental tests on an unstable, pitch-only gimbal setup demonstrate that the linear quadratic regulator can successfully stabilise the system. The experimental results follows the same trend as the predictions from simulation, although additional oscillations are observed that do not appear in the simulated results.

1 INTRODUCTION

Engineers have drawn inspiration from the remarkable ability of insects and hummingbirds to recover from collisions and execute agile manoeuvres, leading to flapping-wing micro aerial vehicles (FWMAV). These drones mimic the characteristic front-to-back wing motion seen in their biological counterparts. Beyond agility, flapping-wing drones also offer improved safety compared to conventional rotary-wing aircraft. Their lightweight wings operate at lower frequencies than rotor blades resulting in less harmful collisions for both the drone and its surroundings.

Recent research on flapping-wing drones has yielded functional prototypes across a wide range of scales. At the larger end of the spectrum, the Flapper Nimble+ is a commercially available platform with a wingspan of 49 cm [1]. At the opposite extreme, the Robobee, with a wingspan of only 3.5 cm, is situated at the insect scale [2]. Between these scales, a number of hummingbird-sized drones with wingspans ranging from 15 to 25 cm have been developed [3, 4, 5]. A key challenge with insect-like flapping-wing flight is its inherent instability. Both in the longitudinal and lateral planes unstable oscillatory modes are present [6]. Active control is essential to stabilise the drone during flight. Nature offers several strategies, for example, insects and hummingbirds can shift their centre of gravity and modulate their wing motion to generate control torques. This paper investigates another mechanism used by hummingbirds: a tail [7]. Positioned underneath the wings, the tail can be angled to redirect airflow, which in turn produces a control torque. In addition, aerodynamic drag acting on the tail generates damping forces that can contribute to passive flight stability.

Previous studies have demonstrated that incorporating a tail into an FWMAV, either as an active control surface or as a passive stabilising element, can improve flight stability and facilitate trajectory tracking [8, 9, 10, 11, 12]. Existing approaches typically rely on largely empirical descriptions of tail-wake interactions combined with conventional PID-based controllers. As a result, the relative effectiveness of different modelling assumptions and control strategies has not yet been systematically established.

This work further explores the use of an active tail on a hummingbird-scale flapping-wing drone. The analysis focuses on the KUlibrie platform, developed at KU Leuven, which has a wingspan of 195 mm and a mass of 15.8 g [13]. This paper establishes an aerodynamic tail model for an FWMAV and integrates it into a free flight simulation of the KUlibrie. This simulation is used to design and validate a tail movement strategy capable of stabilising the drone pitch angle and controlling its position. A linear quadratic regulator (LQR) approach is applied for pitch stabilisation, which is experimentally validated on a test setup that only allows the drone to move around its pitching axis.

2 KULIBRIE DRONE PLATFORM

Figure 1 shows a render of the current prototype of the KUlibrie equipped with a tail. The wings consist of a Mylar foil attached to a carbon fibre frame, and are driven by a resonant actuation system [14]. Two DC motors independently drive the wings through a gear transmission. At the base of each wing, a torsion spring recovers kinetic energy by storing it as potential energy during stroke reversal and releasing it to support the subsequent stroke. To improve efficiency, the motors operate close to the system natural frequency, resulting in resonant wing motion. In the case of the KUlibrie, this resonant flapping frequency is 20 Hz.

*Email address: arno.melis@kuleuven.be

The tail of the KUlibrie is actuated directly by a servo MASRTER DS 208 motor, which only allows tail rotation around the motor axis, parallel with the pitch axis. The tail surface is constructed from ROHACELL 51, a lightweight foam. The tail chord length varies along its span, with the largest chord located near the tips. This region underneath the wing tips experiences the strongest downward airflow generated by the flapping wings [13], resulting in higher aerodynamic force production when the tail surface is located there. The tail is mounted at 2.5 wing chord lengths behind the leading edge of the wings. The tail adds a mass of m_t = 5.2 g to the KUlibrie weight (1.7 g due to the motor, 1.1 g due to the tail surface, 2.4 g due to connection parts).
Wing and tail actuation are controlled by a SEEED XIAO nRF52840 Sense microcontroller, which incorporates a 3-axis gyroscope and a 3-axis accelerometer to estimate the drone attitude.

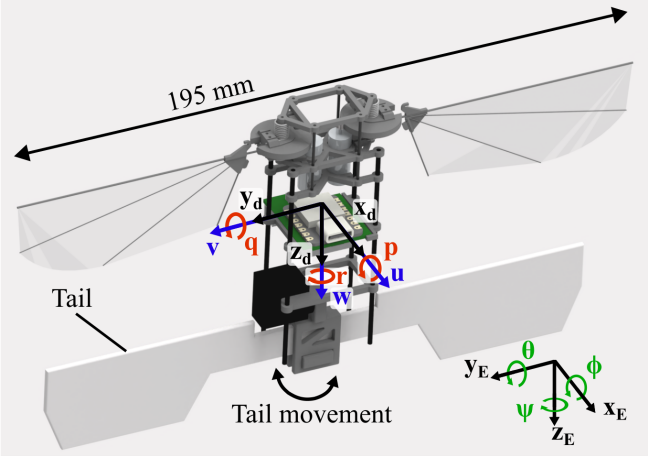

Figure 1: Render of the KUlibrie prototype with tail, with indication of body (x_d, y_d, z_d) and earth (x_E, y_E, z_E) coordinate system together with the velocity (u, v, w), angular velocity (p, q, r) and attitude (ϕ, θ, ψ) components

3 Flight Model

The flight model of the KUlibrie with tail describes the drone motion as the combined result of wing and tail actuation. It is based on the Newton's equations of motion, which determine how the drone velocity and position evolve under the influence of external forces. Following standard aircraft conventions, all kinematic and dynamic quantities are expressed in a body-fixed coordinate system attached to the drone. Figure 1 illustrates this coordinate frame, denoted (x_d, y_d, z_d), where the x_d-axis points forward along the body, the y_d-axis points to the right wing, and the z_d-axis points downward. Drone velocity components (u, v, w), angular velocity components (p, q, r), force components (X, Y, Z), and moment components (L, M, N) are all defined in this reference frame.

The longitudinal equations of motion in this body-fixed frame are given by:

$$\dot{u} = -qw + \frac{X_{\text{wings}}}{m} + \frac{X_{tail}}{m} - g\sin\theta, \tag{1}$$

$$\dot{w} = qu + \frac{Z_{\text{wings}}}{m} + \frac{Z_{tail}}{m} + g\cos\theta, \tag{2}$$

$$\dot{q} = \frac{M_{\text{wings}}}{I_y} + \frac{M_{tail}}{I_y}, \tag{3}$$

$$\dot{\theta} = q. \tag{4}$$

Here, I_y is the moment of inertia around the pitching axis (y_d), m the drone mass and g the gravitational acceleration. The forces and moments are decomposed into contributions from the wings and the tail.
These differential equations are implemented in simulation using a forward Euler integration scheme with a 1 ms time step. At each simulation time step, the aerodynamic models for the wings and tail compute their respective forces and moments, which are applied in the equations of motion to update the drone's velocities and orientation.

3.1 Wing Forces

A model based on the work of Wang et al. [15] determines the forces on the wings. The model is quasi-steady, meaning that wing forces only depend on the current velocity of the wing. It is also a blade element model, meaning that the wing is divided into thin chordwise sections and aerodynamic force contribution is calculated at each section. Figure 2 qualitatively illustrates such a chordwise element. In this study, the blade elements have a 0.1 mm width, and the aerodynamic force is assumed to be perpendicular to the wing surface. Previous research using the KUlibrie has already validated this model both using fluid simulations and experimental measurements [13, 16].

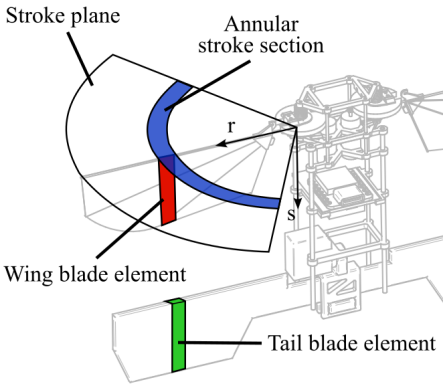

Figure 2: Illustration of a blade element of the wing and tail, together with the stroke plane sections

http://www.imavs.org/

http://www.imavs.org/

3.2 Tail Forces

The forces on the tail are calculated in two steps, first the local downwards velocity of the air at the tail is estimated, and second, the force on the tail is estimated based on this local air velocity.

The velocity field of the air underneath the wings is estimated using actuator disc theory. This method uses the upward force on the wings to estimate the downward velocity imparted on the air, using momentum theory. Previous works used the entire stroke plane (cf. Figure 2) as the actuator disc [17], yielding the following expression for the downwards velocity component of the air underneath the wing:

$$V_z = \sqrt{\frac{T}{2\rho S}}. \tag{5}$$

With V_z the downward velocity component of the air, T the upward thrust generated by the wings, ρ the air density and S the total area of the stroke plane.

For a more detailed estimate of the downward velocity, the approach in this paper splits up the stroke plane up into annular contributions (cf. Figure 2). The upward force generated within each annular section is calculated using the blade element model of the wing forces. The local downward velocity component is:

$$V_z(r) = \sqrt{\frac{dT}{2\rho dS}}. \tag{6}$$

With dT the thrust generated by the annular wing section encompassed by the area dS, and located a distance r from the rotation point of the wing.

The previous formulations give the vertical air velocity at the wing leading edge. To estimate the velocity lower down at the tail position, actuator disc theory predicts that the velocity component rises until it has doubled its value at the leading edge. However, experimental measurements of the downward flow beneath flapping wings indicate that this evolution is no longer accurate beyond approximately two wing chord lengths below the wings [13, 18]. Moving further downwards, the downward velocity component becomes smaller. To implement this velocity profile in the model, a scaling factor of the maximum velocity is added based on experimental measurements on the KUlibrie. This gives the following model:

$$V_z(r, s) = \Omega(s)\sqrt{\frac{dT}{2\rho dS}}. \tag{7}$$

With s the vertical distance to the leading edge of the wing (cf. Figure 2), and Ω the scaling factor established from the measurements conducted in [13]. For the current tail location: $\Omega(2.5\overline{c}) = 1.4$.

A blade element model of the tail divides the tail into chordwise elements to estimate the tail force. The force contribution on each element is calculated using a flat plate model where the lift and drag coefficients are given by:

$$C_L = 2\sin(AoA)\cos(AoA), \tag{8}$$

$$C_D = 2\sin^2(AoA). \tag{9}$$

With AoA the local angle of attack of the tail blade element, resulting from the tail angle, local air velocity and tail velocity.

3.3 Actuation Dynamics

The actuation limits of the tail motor and wing motors are implemented in the simulation. First, the maximum rotation speed of the tail motor of 10 rad/s is prescribed in the simulation. For the wing movement, the simulation does not explicitly account for motor dynamics. Instead, wing motion is assumed to follow a roll-off square wave, as proposed in [19]. To avoid sudden jumps in wing velocity, a change in the stroke amplitude is only applied at the end of each up- or downstroke when the wing is instantaneously stationary. Finally, because the current tail design exceeds the current drone lift capacity, the tail mass in simulation is artificially reduced to the tail motor mass m_t = 1.7 g.

4 CONTROL METHODOLOGY

Figure 3 illustrates the control architecture used in this paper. The drone employs two control actions: adjustment of the tail angle δ_t generates a pitching torque, and modification of the wing stroke amplitude ϕ_m increases thrust. Together, these inputs control two longitudinal degrees of freedom. In this work, the two longitudinal position coordinates (x_E, z_E) are controlled trough a cascaded control structure. The position reference is first processed by the position controller, which outputs a desired velocity $(V_{x,\text{ref}}, V_{z,\text{ref}})$. This velocity reference is transformed into the drone body frame to obtain reference commands for u and w. Each value is sent to its respective controller: the w-controller determines the required stroke amplitude ϕ_m, while the u-controller computes a pitch reference θ_{ref}. This pitch reference is passed to the pitch controller, which calculates the necessary tail deflection δ_t.

4.1 Control Model

The full equations of motion from equations 1 - 4 are useful for simulation purposes, however they are too complex for direct use in controller design. A stroke-averaged linearised formulation makes the system tractable for controller design. This is obtained as follows: the forces are averaged over one stroke period and linearised around hover using their first order Taylor expansion. The movement in the z_E direction can be decoupled, leading to the following state space models [6]:

$$\begin{bmatrix} \dot{u} \\ \dot{q} \\ \dot{\theta} \end{bmatrix} = \begin{bmatrix} \frac{X_u}{m} & \frac{X_q}{m} & -g \\ \frac{M_u}{I_y} & \frac{M_q}{I_y} & 0 \\ 0 & 1 & 0 \end{bmatrix} \begin{bmatrix} u \\ q \\ \theta \end{bmatrix} + \begin{bmatrix} \frac{X_\delta}{m} \\ \frac{M_\delta}{I_{yy}} \\ 0 \end{bmatrix} \delta_t, \tag{10}$$

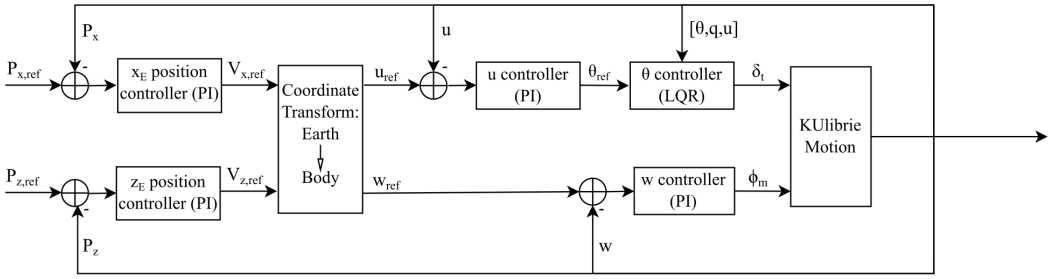

Figure 3: Block diagram of the cascaded controller structure

$$\dot{w} = \frac{Z_w}{m}\, w + \frac{Z_\phi}{m}\, \phi_m. \tag{11}$$

The parameters of this model such as Z_w represent a partial derivative of a stroke-averaged force component (here Z) with respect to a motion component or control input (here w). These quantities, commonly referred to as stability derivatives, each have a physical interpretation. Diagonal elements of the system matrix correspond to damping effects, whereas off-diagonal elements represent coupling between different directions of motion. The model parameters M_δ, X_δ and Z_ϕ describe the influence of the corresponding control actions on the system motion.

Because of the decoupling of w, the control problem can be separated such that the tail angle is used to control θ, while w is controlled through the stroke amplitude. This decoupling justifies the earlier division of the architecture into a w-controller and a θ-controller.

4.2 Pitch Controller Design

The longitudinal dynamics of the drone described by Equations 1 - 4 are unstable, exhibiting an unstable oscillatory mode in both u, θ and q [6]. To counteract this coupled oscillation, a state-feedback controller is employed, more specifically a linear quadratic regulator (LQR). Figure 4a. presents the block diagram of the LQR controller, which uses the system states θ, q, and u as feedback. The feedback matrix K is obtained by minimising the following cost function:

$$J = \int_0^\infty \left(\rho\, \theta^2(t) + \delta_t^2(t)\right)\, dt. \tag{12}$$

ρ is a weighting constant that balances tracking performance and control effort. An extension of the LQR controller is the linear quadratic integral (LQI) controller. Figure 4b. shows the block diagram of the LQI controller. This controller introduces an integral state to reduce steady-state errors. The inclusion of this integral state modifies the optimisation problem as follows:

$$J = \int_0^\infty \rho \left(\theta^2(t) + \alpha \left(\int_0^t e(\tau)\, d\tau\right)^2\right) + \delta_t^2(t)\, dt. \tag{13}$$

The additional weighting factor α determines the trade-off between the instantaneous error penalty and the accumulated error.

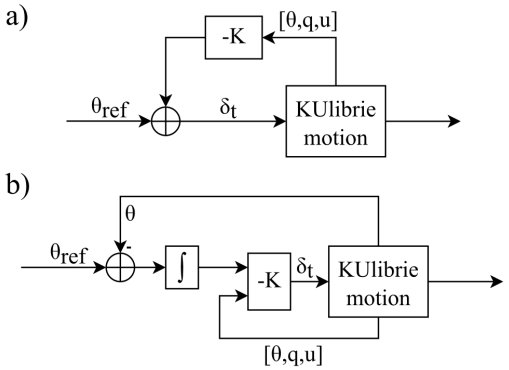

Figure 4: Block diagram of a) an LQR controller and b) an LQI controller

With both control types the state data is first passed through a moving average filter with a period of one stroke cycle before being fed back to the controller. This reduces the effect noise due to body oscillations of the drone. These rapid oscillations at the flapping frequency of the drone were averaged out during controller design, meaning that they represent unwanted noise on the feedback data.

4.3 Velocity and Position Controller Design

With the drone movement stabilised by the pitch controller, the remaining controllers in the architecture, namely the velocity and position controllers, act on systems that are already stable. For these subsystems, standard PI control is selected. The PI gains are tuned manually by balancing reference tracking accuracy against actuator effort, aiming at preventing actuator saturation for the given reference signals. Although the balance between speed and actuator limits depends on the specific application, in this paper the controller gains are adjusted to track a step input on the position to (0.5 m, -0.5 m) as closely as possible.

http://www.imavs.org/

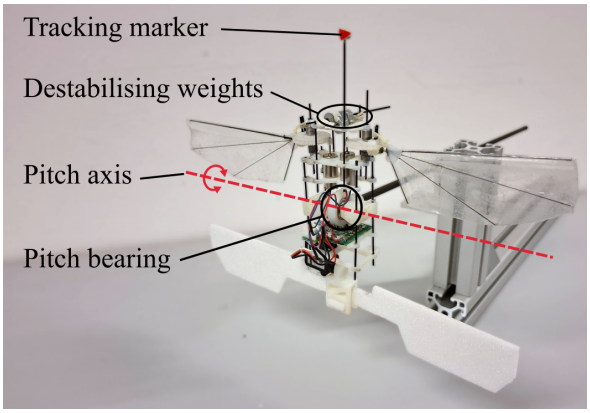

Figure 5: Experimental setup that only allows pitching rotation

4.4 Experimental Pitch Control Setup

Figure 5 shows the experimental setup to validate the LQR approach for pitch control. The KUlibrie is mounted on a ball bearing, restricting all degrees of freedom except the pitch rotation. Added weight on top of the drone moves its centre of gravity 2.1 mm above the fulcrum leading to an unstable system akin to free flight. This setup avoids crashes and isolates the performance of the pitch controller. However, because it only allows pitching movement, it does not fully capture the front-to-back unstable oscillating mode of free flight.

During the experiment θ and q are estimated using the onboard gyroscope and accelerometer together with a Kalman filter, the design of which is discussed in [20]. In addition, drone pitch angle is measured by visual tracking. This data is used after the experiment as an absolute measure for the estimation and tracking performance.

5 Results

5.1 Simulation Results

Figure 6 shows the simulation results of a step reference input of $\theta_{\text{reference}} = 3°$ applied at $t = 6$ s to the LQR pitch controller in free flight for three distinct values of the weighting factor $\rho = \{0.1,1,10\}$. It shows the pitch angle θ and tail angle δ_t of the drone during the free flight simulation. To ease interpretation, in this and following figures, the stroke averaged value of θ is shown. This removes the body oscillations, with an amplitude of about 3°. The results show that for all the displayed values of ρ the LQR controller is able to stabilise the pitch angle of the drone after a start-up transient. As expected, the higher values of ρ track the step input faster, but need larger tail movements. To this end, $\rho = 100$ and higher (not shown in the figure) would not stabilise the start-up transient as the tail actuator saturates. Each of the LQR controllers has a steady-state error due to the differences between the simulation and stroke-averaged linearised system.

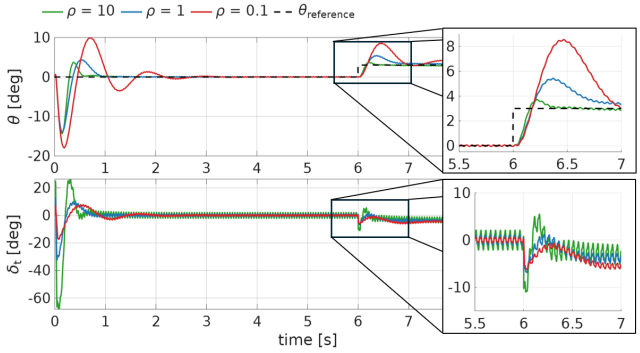

Figure 6: Simulation results of the LQR controller for $\rho = \{0.1, 1, 10\}$. The inserts show a zoom for the time interval [5.5 s; 7.5 s]

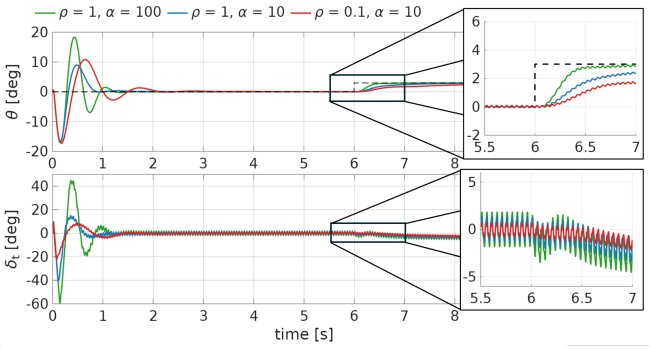

Figure 7: Simulation results of the LQI controller for $\rho = \{0.1, 1\}$ and $\alpha = \{10, 100\}$. The inserts show a zoom for the time interval [5.5 s; 7.5 s]

The results indicate that the steady-state error decreases as the value of ρ increases.

Figure 7 shows the simulation results of the same step reference applied to the LQI controller with various values of ρ and α. After a start-up transient, the LQI controller can also stabilise the free flight system. Again, higher values of ρ and α lead to better tracking performance, but larger tail movements. As opposed to the LQR controller, the LQI controller does not have a steady-state error, due to the integrator.

Figure 8 shows the simulation results of the cascaded control structure tracking a step position input of (0.5 m, -0.5 m), showing that the cascaded structure successfully tracks the reference. The results show that the settling time in the x_E-direction is 5.8 s with an overshoot of 15%. The tracking in the z_E-direction is faster, with a settling time of 3.6 s and no overshoot. Due to the integral action of the PI controller both axis show zero steady state error.

5.2 Experimental Results

Figure 9 and 10 show the experimental results of a ramp input reference of the LQR and LQI controller on the gimbal setup respectively. The ramp input reference goes from 0° to

http://www.imavs.org/

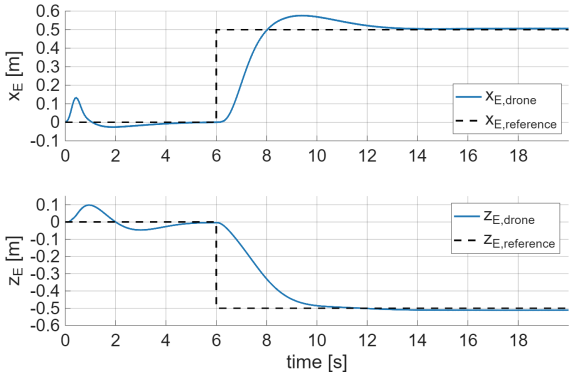

Figure 8: Simulation results of the cascaded controller tracking a (0.5 m, -0.5 m) step input

20° in 2 s. The figures show the estimated pitch angle through the Kalman filter, and the actual pitch angle measured through a camera equipped with visual tracking software. The results show that the Kalman filter estimates the pitch angle with good accuracy. Both the LQR and LQI controllers stabilise the system and track the reference. Despite this, added oscillations are observed, with a maximum amplitude of approximately 10°. The oscillation frequency is significantly lower than the flapping frequency of 20 Hz, suggesting that the pulsating wing forces are not the primary cause. A likely source of these oscillations are modelling errors. For instance, if the rotational damping in the model is underestimated, the resulting controller may be overly aggressive, leading to oscillatory behaviour. Other modelling inaccuracies, such as unmodelled tail motor dynamics or errors in the tail force model, may also contribute.

Comparing controller parameters, larger values of ρ and α result in a faster response, as expected. However, for $\rho = 10$ and $\alpha = 10$, the increased controller aggressiveness leads to larger oscillations. Conversely, lower values of ρ or α yield a slower response. In particular, the performance of the LQR controller with $\rho = 0.1$ is significantly degraded due to the system's slow reaction time.

Figure 11 shows the comparison of the experimental results, the prediction from the linear system and from the simulation. It shows that the linear system and the simulation are almost identical, differing by the simulation having a start-up transient. The experimental result shows roughly the same evolution as the simulation, however it has the added oscillations on top.

6 Study Limitations

The wing force model employed in this work is based on a quasi-steady blade element formulation, which assumes rigid wings and neglects three-dimensional aerodynamic effects. Although this modelling approach has been validated

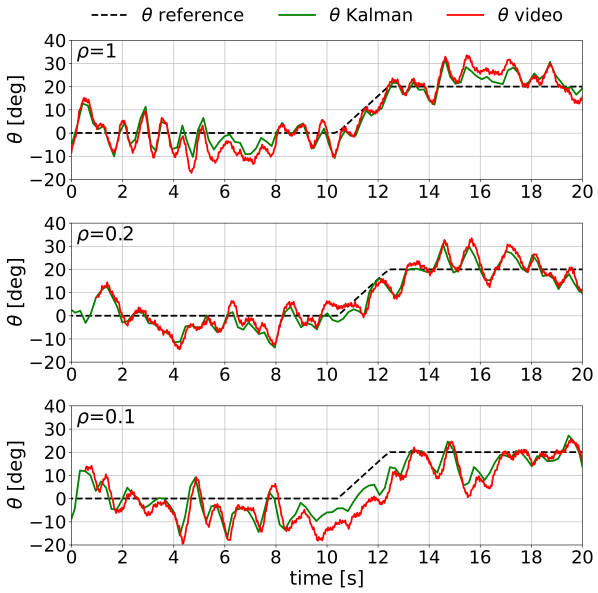

Figure 9: Experimental results of the LQI controller to a ramp input for values of $\rho = \{1, \frac{1}{5}, \frac{1}{10}\}$

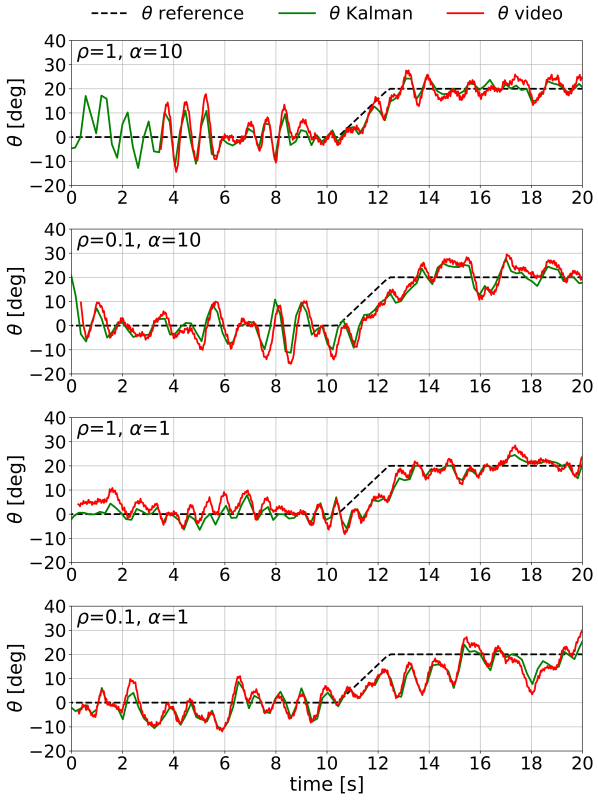

Figure 10: Experimental results of the LQI controller to a ramp input for $\rho = \{0.1, 1\}$ and $\alpha = \{1, 10\}$

http://www.imavs.org/

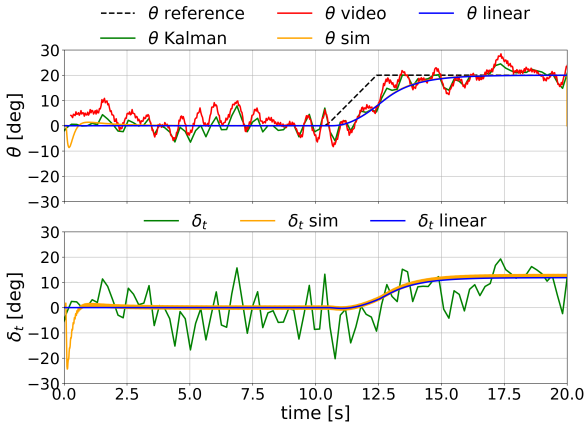

Figure 11: Comparison of the experimental, linear system and simulation results of the LQI controller

in both fluid simulations and static experiments [13, 16], the influence of forward flight velocity and wing deformation remains uncertain. The tail force model is founded on similar assumptions and additionally relies on actuator disc theory, which neglects vortex structures in the wake of the drone. Further detailed validation of this model is therefore required. Finally, while the pitch control strategy is experimentally validated in this study, the complete cascaded control architecture has yet to be validated experimentally.

7 Conclusion and Future Work

This paper analyses the longitudinal control of a hummingbird-inspired flapping-wing drone equipped with an active tail. The proposed tail is mounted beneath the wings and is directly actuated by a servo motor. A cascaded control architecture is explored, in which the position and velocity loops are implemented using PI controllers, while pitch control is achieved using a linear quadratic regulator. Controller gains are derived from a stroke-averaged, linearised free-flight model. The resulting controllers are evaluated in simulation using an actuator disc approach combined with a quasy-steady blade element method. Simulation results show that the LQR controller stabilises the system and tracks a step reference in pitch. However, differences between the stroke-averaged linear model and the higher-fidelity simulation introduce a steady-state error in pitch tracking. Augmentation of the LQR controller with integral action removes this steady-state error. Simulations of the complete cascaded control loop demonstrate that the system is capable of tracking a position reference of (0.5 m, -0.5 m).
Experimental validation of the pitch control strategy is performed using a gimbal setup that restricts the system to pitch motion only, with additional mass added to the drone to induce instability. The results demonstrate that the LQR controller is capable of stabilising the system. The measured responses exhibit trends similar to those observed in simulation, but with additional oscillations, which are likely caused by modelling errors. The next step for improving controller performance is to carry out system identification experiments for both stationary and free-flight conditions, in order to improve model fidelity and support more accurate controller design.

Acknowledgements

This work was financially supported by the Fonds Wetenschappelijk Onderzoek - Vlaanderen (FWO), grant numbers G021225N, 1SA2U26N

References

[1] Flapper Drones. Flapper nimble+: Bioinspired flying development platform. https://flapper-drones.eu/nimbleplus/, 2026. Accessed: 2026-07-14.

[2] Pakpong Chirarattananon. *Flight Control of a Millimeter-Scale Flapping-Wing Robot*. Phd dissertation, Harvard University, 2014.

[3] Quoc-Viet Nguyen and Woei Leong Chan. Development and flight performance of a biologically-inspired tailless flapping-wing micro air vehicle with wing stroke plane modulation. *Bioinspiration & Biomimetics*, 14(1):016015, 2019.

[4] Zhan Tu, Fan Fei, Jian Zhang, and Xinyan Deng. An at-scale tailless flapping-wing hummingbird robot. i. design, optimization, and experimental validation. *IEEE Transactions on Robotics*, 36(5):1511–1525, 2020.

[5] Hoang Vu Phan, Steven Aurecianus, Taesam Kang, and Hoon Cheol Park. Kubeetle-s: An insect-like, tailless, hover-capable robot that can fly with a low-torque control mechanism. *International Journal of Micro Air Vehicles*, 11:1756829319861371, 2019.

[6] M. Sun. Insect flight dynamics: Stability and control. *Reviews of Modern Physics*, 86(2):615–646, 2014.

[7] D. L. Altshuler, M. Princevac, H. Pan, and J. Lozano. Wake patterns of the wings and tail of hovering hummingbirds. *Experiments in Fluids*, 46:835–846, 2009.

[8] Kai Hu, Huichao Deng, Shengjie Xiao, Gongyu Yang, and Yuhong Sun. Design of a bio-inspired, two-winged, flapping-wing micro air vehicle with high-lift performance. *Journal of Bionic Engineering*, 21(3):1191–1207, 2024.

[9] Hussein Altartouri, A Roshanbin, G Andreolli, L Fazzi, Matej Karásek, Mohamed Lalami, and André Preumont. Passive stability enhancement with sails of a hovering flapping twin-wing robot. *International Journal of Micro Air Vehicles*, 11:1756829319841817, 2019.

http://www.imavs.org/

[10] Zhi Ern Teoh, Sawyer B Fuller, Pakpong Chirarattananon, N. O. Prez-Arancibia, Jack D Greenberg, and Robert J Wood. A hovering flapping-wing microrobot with altitude control and passive upright stability. In *2012 IEEE/RSJ international conference on intelligent robots and systems*, pages 3209–3216. IEEE, 2012.

[11] Shengjie Xiao, Yuhong Sun, Dapeng Ren, Kai Hu, Huichao Deng, Yun Wang, and Xilun Ding. Design and flight performance of a bio-inspired hover-capable flapping-wing micro air vehicle with tail wing. *Aerospace*, 10(11):910, 2023.

[12] Yichen Zhang, Yiming Xiao, Qingcheng Guo, Feng Cui, Jiaxin Zhao, Guangping Wu, Chaofeng Wu, and Wu Liu. Stability and controller research of double-wing fmav system based on controllable tail. *Biomimetics*, 9(8):449, 2024.

[13] T. Roelandt. *Flapping Wing Nano Drones in Hovering Flight: Vehicle Design and Analysis of Flight Performance*. PhD thesis, KU Leuven, Leuven, Belgium, 2025.

[14] S. Timmermans. *Flight Performance of Nano Aerial Vehicles with Flapping Wings: Experiment-Based System Modelling*. PhD thesis, KU Leuven, Leuven, Belgium, 2021.

[15] Q. Wang, J. F. L. Goosen, and F. Van Keulen. A predictive quasi-steady model of aerodynamic loads on flapping wings. *Journal of Fluid Mechanics*, 800:688–719, 2016.

[16] Thomas Roelandt, Arno Melis, Jeroen Vanpoucke, Giheon Ha, Hoon Cheol Park, and Dirk Vandepitte. Comparison of stroke and stroke plane modulation in insect-like flapping wing forward flight control. In *2026 New Trends in Civil Aviation (NTCA)*, pages 15–22. IEEE, 2026.

[17] L. Wang, W. Jiang, L. Zhao, and Z. Jiao. Modeling and hover flight control of a micromechanical flapping-wing aircraft inspired by wing–tail interaction. *IEEE/ASME Transactions on Mechatronics*, 28(6):3132–3142, 2023.

[18] L. Zhao, W. Wang, Y. Chen, and Z. Jiao. Analytical modeling of a hoverable x-shape flapping wing aircraft considering wing–tail interaction. In *Proceedings of the 32nd Congress of the International Council of the Aeronautical Sciences (ICAS)*, pages 1–11, 2021.

[19] M. Karásek. *Robotic hummingbird: Design of a control mechanism for a hovering flapping wing micro air vehicle*. PhD thesis, Universite libre de Bruxelles, Bruxelles, Belgium, 2014.

[20] B. Helsen, T. Roelandt, M. Floren, and D. Vandepitte. Flight control of an insect-like tailless flapping wing nano-robot around hover. In *Proceedings of the 15th Annual International Micro Air Vehicle Conference and Competition*, pages 23–32, 2024.

http://www.imavs.org/